# Magnetomechanical Four-State Memory

*Chad S. Watson,* Courtney Hollar, Kimball Anderson, William B. Knowlton, and Peter Müllner*

**With current non-volatile memory technology approaching intrinsic storage density limits, new data storage technologies are under development. Probe-based storage systems provide alternatives to conventional mass storage technologies. Ni-Mn-Ga, a ferromagnetic shape memory alloy (FSMA), is proposed as a medium for multi-bit storage using scanning probe microscopy (SPM) techniques. Local modifications of the magnetic stray field were achieved using nanoindentation. Magnetic poles collect within the indentation, which is leveraged to control the magnetic stray field for the patterning of magnetic information. Four magnetic-based memory states are possible due to magnetic field or stress-induced twin rearrangement along two crystal orientations, each with two possible magnetic orientations.**

## 1. Introduction

Ultrahigh density data storage requires materials with non-volatile memory states that exhibit predictable switching thresholds. In the case of probe-based storage, the interaction of a nanometer sharp probe with the storage medium enables the reading, writing and erasing of data. Storage mechanisms include topology (thermomechanical indentations),[1] polarization (tip-sample electrical field)[2] and electrical resistance (phase change)[3] depending on the storage medium (polymer, ferroelectric and chalcogenide material systems). Thermomechanical data storage, using polymer material systems, is the most mature where storage densities of 4 Tb/in$^2$ have been demonstrated.[4] For thermomechanical storage, a heated probe comes into contact with the polymer medium and creates an indentation, which represents a logical 1. The same probe senses (reads) the change in topography due to the indentation. Changes in topography as a mechanism for storing data have also been applied to conventional shape memory alloys using nanoindentation,[5] where a diamond probe was used to induce indentations on a thin film of nickel-titanium. The indentation partially recovered by heating from the martensite phase into the austenite phase. Plastic deformation, by lattice dislocations, restricted complete recovery. While providing enhanced storage density capacities, the constraint of two bits per cell limits the long term potential of these techniques. With the use of Ni-Mn-Ga as the storage medium, we can attain additional levels of information within each bit through nanonindentation-induced changes in the local magnetic stray field.

Ni-Mn-Ga alloys exhibit large plastic strains of up to 10% when exposed to a magnetic field (direct effect) or stress (inverse effect).[6–10] While the strains are plastic, by inducing a permanent macroscopic shape change, the original shape can be recovered thermoelastically or with an externally applied magnetic field. Twin boundary motion accommodates the large magnetic-field-induced strains (MFIS) resulting in the growth of martensite variants that contain magnetic moments preferentially aligned to the applied field. In the case of stress-induced compressive deformation, martensite variants with the axis of easy magnetization (the crystallographic *c* direction) parallel to the applied stress grow, thus changing the total magnetization. This stress induced change in magnetization can be leveraged for memory and sensor applications.

Twinning, as the primary deformation mechanism of Ni-Mn-Ga, is achieved with applied compressive stresses as low as 0.1 MPa for high-purity alloys that exhibit twinning mode II. Impurities and twinning mode I lead to higher twinning stresses.[9,11] Microscopically, twin boundaries host a series of twinning disconnections.[12] The disconnections, line defects in the crystal interface, generate a local stress field at the twin boundary. Twin boundary motion induced by a mechanical stress is the result of the interaction of the macroscopic stress field with the stress concentration of the disconnection. At a critical stress, disconnection motion, thus twin boundary motion, occurs. Thus, by inducing plastic deformation at the nanoscale, local changes in magnetization may proceed.

While stress-induced deformation and corresponding changes in magnetization have been well established at the macroscopic and mesoscopic scales,[8,13–16] research linking nanoscale deformation to changes in local magnetic properties has received less attention. A majority of the work at the nanoscale has been focused on nanomechanical properties and deformation behavior as a function of composition, surface condition or twin orientation.[17–21] The work presented here

C. S. Watson, C. Hollar, K. Anderson,
Prof. W. B. Knowlton, Prof. P. Müllner
Department of Materials Science & Engineering
Boise State University
Boise, ID 83725, USA
E-mail: chadwatson1@boisestate.edu
C. Hollar, K. Anderson
Department of Mechanical & Biomedical Engineering
Boise State University
Boise, ID 83725, USA
Prof. W. B. Knowlton
Department of Electrical & Computer Engineering
Boise State University
Boise, ID 83725, USA

**DOI: 10.1002/adfm.201203015**

provides insight into deformation mechanics and the magnetic response of a ferromagnetic shape memory alloy (FSMA) at the nanoscale. We performed nanoindentation, atomic force microscopy (AFM) and magnetic force microscopy (MFM) with a scanning probe microscope to indent and to measure topography and magnetic structure. We created nanoindentation arrays to evaluate the effect of indentation spacing and size on the magnitude and morphology of the local magnetic stray field. The stresses associated with nanoindentation using a sharp diamond probe resulted in plastic deformation, through a combination of lattice dislocations and twinning disconnections, which changed the local magnetic structure sensed using MFM. We demonstrate that indentation load, spacing, and size control the local magnetization. The ability to tune local stress to control local magnetization can be leveraged for the patterning of magnetic information for memory applications.

## 2. Results and Discussion

A series of 5 × 5 arrays of indentations were made on the polished {100} face of the Ni-Mn-Ga single crystal. For these arrays, indentation loads ranged from ≈5 to 26 μN with spacings from 25 to 200 nm. Following indentation, AC mode and constant height imaging were performed using CoCr coated silicon cantilevers. Corresponding topography and MFM phase images are shown in **Figure 1**. Prior to indentation, the entire surface exhibited neutral contrast. Neutral contrast indicates that the magnetization, thus the *c*-axis (due to the high magnetocrystalline anisotropy of Ni-Mn-Ga), is parallel to the surface. For regions plastically deformed by nanoindentation, the MFM image reveals a localized change in the magnetic stray field from neutral to strong contrast (black and white). Out-of-plane magnetization consists of the magnetic stray field directed into (black) or out of (white) the surface.

For the 26 μN/200 nm indentation array in Figure 1b, each indentation resulted in a distinct dark and bright region. Along the horizontal direction, the dark and bright regions tended to merge such that a continuous dark/bright response formed for each row of indentations. When the spacing was reduced, from 200 to 100 nm, a change in the local magnetic contrast occurred. Instead of each row exhibiting a relatively consistent dark and bright contrast, an apparent coupling occurred within the array. The top and bottom row showed enhanced magnetic contrast while the middle rows exhibited a muted dark/bright response. The magnitude of the dark and bright regions was intensified compared to the 26 μN/200 nm array. Decreasing the load from 26 to 13 and 10 μN resulted in a change in magnetic contrast similar to that of the 26 μN/200 nm array: continuous dark and bright contrast for each row of indentations. Reducing load and spacing further to 7.5 and 6.5 μN and to 50 nm resulted in a magnetic response similar to that of the 26 μN/100 nm array. Here, the contrast was more significant at the bottom and top rows of the array, and the intermediate rows exhibited reduced dark/bright contrast. From this series of indentation arrays shown in Figure 1b, five major trends arose: i) each indentation resulted in both dark and bright contrast, ii) a directionality of dark to bright contrast existed, where dark contrast was below the bright contrast, iii) as the indentation load decreased, the magnitude of the magnetic contrast decreased, iv) indentation induced magnetic stray fields coupled to neighboring stray fields and v) the top and bottom edge of small pitched arrays had an enhanced dark/bright contrast.

Because of the high magnetocrystalline anisotropy of Ni-Mn-Ga, the dark and bright regions of contrast in the MFM images are typically indicative of domains within a martensite variant with the *c*-axis normal to the sample surface. Thus, the strong contrast in the indents may indicate stress-induced twinning that switches the crystallographic *c* direction (i.e., the easy axis of magnetization) from parallel to the surface to perpendicular to the surface. To examine the validity of the stress-induced twinning hypothesis, the Ni-Mn-Ga sample was heated to the austenite phase and held at 75 °C for 20 min, cooled to room temperature and then re-imaged. By cycling through the martensitic phase transition, stress-induced twins recover thermoelastically. If twinning caused all the deformation, the indentation would not conform to the indenter geometry, but instead exhibit the appropriate surface relief consistent

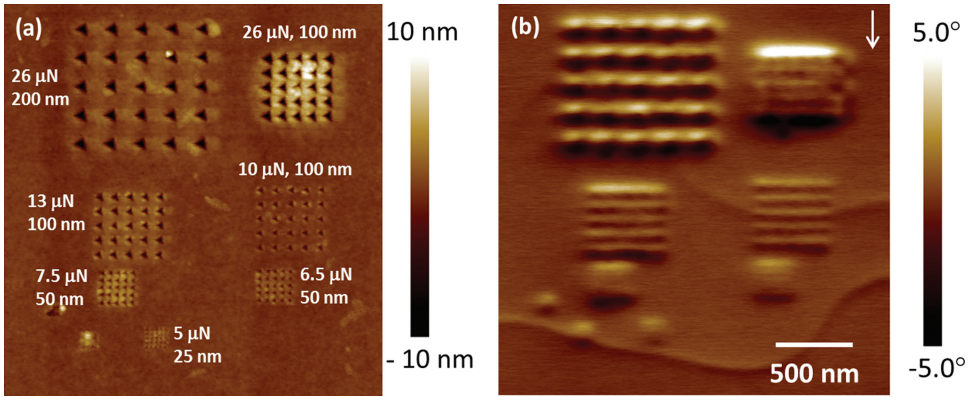


**Figure 1.** a) AFM topography and b) MFM phase image of 5 × 5 indentation arrays showing the patterning of magnetic information on Ni-Mn-Ga using nanoindentation. The indentation loads range from 5 to 26 μN with a separation between indentations ranging from 25 to 200 nm. The *c*-axis is parallel to the sample surface with the magnetization direction indicated by the white arrow. The indentation arrays exhibit a dark/bright magnetic contrast which indicates a change from in-plane, magnetization (neutral contrast) to out-of-plane magnetization (strong contrast). The scale bar in (b) applies to both images.

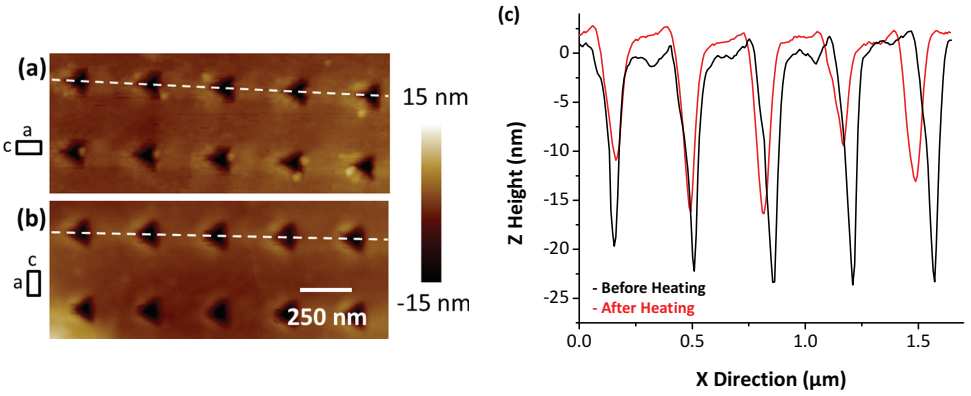


**Figure 2.** a) AFM topography image of 26 μN/300 nm array before heating to above the martensitic phase transformation temperature. b) AFM topography image of the same array after heating and cooling through the martensitic phase transformation. Both images were captured at room temperature. c) Cross-section of indentations before and after heating indicated by dashed lines in (a) and (b). The difference in indentation depth is due to thermoelastic recovery of twins. The shift in the indentation locations is due to the formation of self-accommodating martensitic twins forming during cooling. A new twin, encompassing the indentations, formed with the *c*-axis parallel to the long axis of the image. Originally, prior to heating/cooling, the *c*-axis was parallel to the short axis of the image.

with the 10M martensite Ni-Mn-Ga twinning angle, and fully recover upon heating and cooling. **Figure 2** shows a portion of a 26 μN/300 nm array before (Figure 2a) and after (Figure 2b) heating through the martensitic phase transformation. Prior to heating, the indentation depth, based on averaging the maximum depths for each of the 10 indentations, was 21.9 ± 2.2 nm. Upon cooling to room temperature from 75 °C, the indentations partially recovered to a depth of 15.0 ± 2.7 nm. A line scan in Figure 2c demonstrates the difference in indentation depths. On average, the indentations recovered 31% upon cycling through the martensitic phase transformation. Thus, the deformation induced by indentation was attributed to both lattice dislocations and twinning. This is evident by the incomplete recovery of the indent; the indent remnant is permanently deformed due to lattice dislocations. The magnetic contrast persisted, even after being thermoelastically recovered. Therefore, localized stress-induced twinning did not significantly contribute to the local magnetic stray field.

The modification of the local magnetic stray field is not related to deformation twinning; rather, the magnetic contrast in the MFM images were the result of creating new surfaces for magnetic poles to collect. Similar to the principles of magnetic particle inspection[22] and the Bitter method,[23] where magnetic stray fields facilitate the imaging of magnetic inhomogeneities (e.g., cracks and domain walls), MFM senses the local magnetic stray fields. On the nanoscale, the indentations disrupt the magnetic flux lines parallel to the surface. This disruption results in the formation of positive and negative magnetic poles on opposite sides of the plastically deformed regions, which modifies the local stray field (**Figure 3**a).[24] The probe, with a magnetization vector pointing toward the sample surface, is repelled from the positive poles causing bright contrast. Negative poles attract the probe and cause a dark contrast. The location of positive and negative magnetic poles that collect within topological features, such as scratches and indentations, depends on the direction of the magnetization vector within the sample.[24–26]

The MFM images in Figure 3b,c provides an instructive demonstration of the relationship between the magnetization vector and the orientation of the dark/bright contrast. A load of 128 μN with a period of 500 and 750 nm created the arrays in Figure 3b. For the arrays in Figure 3c, with a constant pitch of 500 nm, the indentation load varied from 12.8 to 76.8 μN. The MFM images show a variety of magnetic features: i) spike domains, which have recently been characterized for Ni-Mn-Ga,[27] ii) out-of-plane and in-plane twin variants, iii) a 180° domain wall, and iv) indentation and scratch induced changes in magnetization. The magnetic features emanating from the out-of-plane to in-plane twin boundary are a form of spike domains (Figure 3b). Spike domains form 180° domain walls to minimize magnetostatic energy and are typically associated with pinning sites (inclusions, pores, chemical inhomogeneities, grain boundaries), surfaces that are slightly tilted from the crystallographic easy axis of magnetization, and twin boundaries.[27–29] The intersection of indentation arrays with the spike domains resulted in a reversal of the dark/bright contrast direction. The reversal was caused by the switching of positive and negative magnetic poles. Similarly, an indentation array intersected an in-plane 180° domain wall (Figure 3c) exhibiting a corresponding change in the directionality of the dark/bright contrast. On one side of the array, for each indentation, the dark/bright contrast was from bottom to top and on the opposite side of the array, the contrast was from top to bottom. Indentation arrays on either side of the 180° domain wall exhibited the same phenomenon.

The switching of the dark and bright contrast, as a function of magnetization direction, provides the basis for establishing a multi-state memory device using Ni-Mn-Ga as the medium. Magnetic information is stored, by way of the magnetic poles, about the locally deformed region. The magnitude and morphology of the magnetic information can be manipulated by indentation spacing and load. An apparent coupling of the magnetic stray fields emanating from the indentations resulted in the formation of linear regions with a persistent stray field, herein referred to as perpendicular coupling (because the coupling occurs normal to the *c*-axis), of dark or bright contrast (Figure 1, 3 and **Figure 4**). For arrays with an indentation spacing

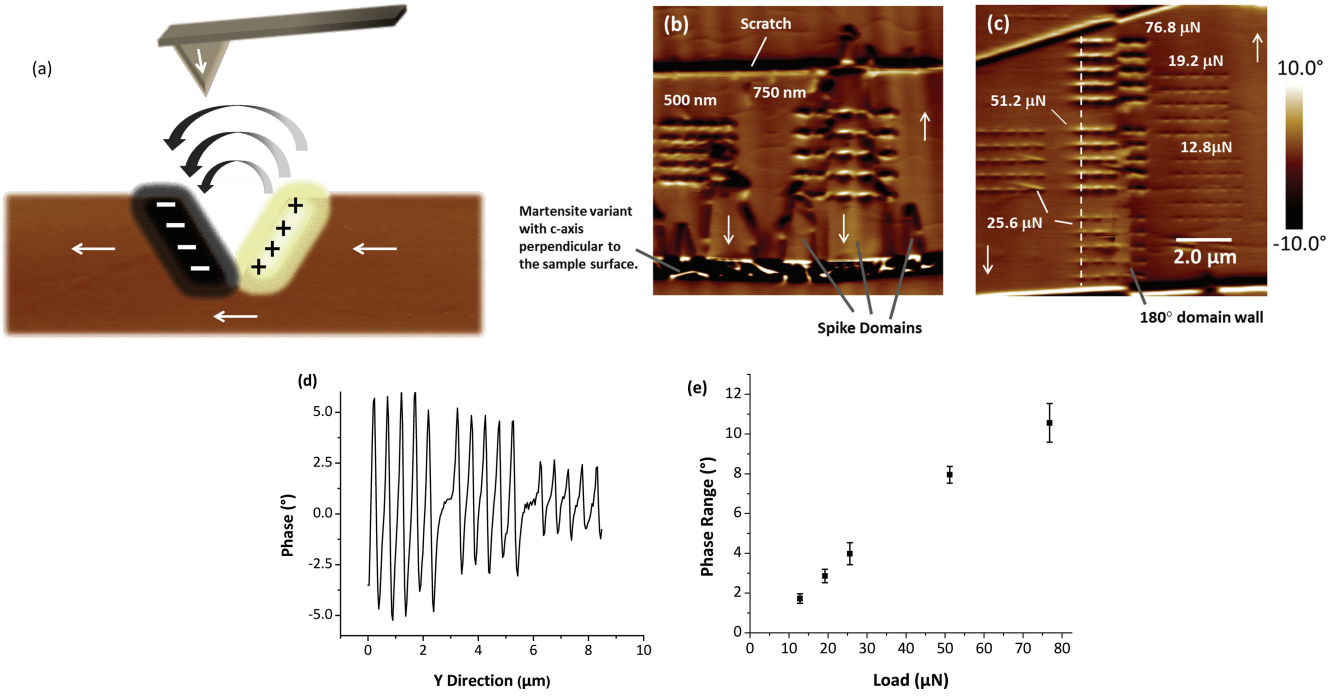


**Figure 3.** a) Cross-section schematic of an indentation, the formation of positive and negative poles, and the resulting magnetic stray field sensed with a CoCr coated silicon cantilever. The magnetization vector points to the left, resulting in a bright contrast on the right and dark contrast on the left of the indentation. b) MFM phase image of arrays formed with an indentation load of 128 μN and a spacing of 500 and 750 nm. The twin with the *c*-axis perpendicular to the sample surface exhibits a maze pattern of dark/bright contrast associated with 180° magnetic domains perpendicular to the surface. Spike domains, emanating from the out-of-plane to in-plane twin boundary, rotate the local magnetic stray field 180° from the prevailing in-plane magnetization direction. c) MFM phase image of arrays with a constant pitch of 500 nm and loads ranging from 12.8 to 76.8 μN showing the relationship between indentation load and the magnitude of the phase contrast. d) Phase shift cross-section, indicated by the dashed line in (c), for applied loads of 76.8, 51.2, and 25.6 μN. e) Relationship between applied load and magnetic contrast for all arrays shown in (c). The scale bar in (c) also applies to (b).

of 500 nm, (Figure 3c) indentation loads of 12.8, 19.2 and 25.6 resulted in each indentation exhibiting a distinct dark/bright contrast (i.e., coupling perpendicular to the crystallographic *c* direction was not observed). However, at a load of 51.2 μN, coupling perpendicular to the magnetization direction became evident and more prevalent for the array formed with a 76.8 μN load. As the indentation spacing was decreased (at a constant load of 26 μN) from 200 to 100 nm (Figure 4a,b), a second coupling phenomenon occurred, in which the magnetic poles appear to accumulate at the top and bottom of the indentation array, resulting in a magnetic stray field with an enhanced dark and bright contrast. The enhanced coupling became even more pronounced as the indentation spacing decreased from 100 to 50 nm (Figure 4b,c).

Contributions from the MFM probe, due to spatial resolution limitations, result in the averaging of stray fields emanating from closely spaced indentations. For the probes used in this study, the spatial resolution is between 50 and 100 nm. The estimation in spatial resolution is based on the contrast observed in Figure 1b. For instance, the dark/bright contrast associated with each row of indentations with 100 nm spacing at 10 and 13 μN loads are resolvable. The ability to resolve the dark/bright contrast at an indentation spacing of 50 nm and load of 6.5 μN is marginal. Based on this interpretation, the contributions to the reduced contrast for the interior rows in the 100 nm spacing, 26 μN load array (Figure 1b) are not explicitly related to spatial resolution limitations, but rather a form of magnetostatic coupling. The enhanced contrast for the outer rows of the 100 nm spacing, 26 μN load array and the enhanced contrast exhibited by the 50 nm, 26 μN load array (Figure 4c) substantiate this claim.

Magnetostatic coupling has been observed in isolated ferromagnetic single domain islands[30–34] and employed to demonstrate geometrically frustrated lattices composed of nanoscale ferromagnetic islands[32] and magnetic quantum-dot cellular automata for potential magnetic memory and logic applications.[30,34] The coupling, due to the formation of magnetic poles and the forces associated with magnetic stray fields, influences the magnetic moment of neighboring islands. For Ni-Mn-Ga, the coupling effect could potentially be engineered to perform memory and logic functions. In principle, by manipulating indentation load and spacings, a magnetomechanical switch could be designed that would enable coupling for nanoscale information processing.

In the case of ultrahigh density data storage, to minimize the susceptibility to magnetostatic coupling, the indentation load can be adjusted for a particular spacing. As the indentation load increased, the magnitude of the magnetic contrast in the MFM images increased (Figure 3c). Figure 3d shows a cross section of the magnetic contrast for a column of indentations formed by an applied load of 76.8, 51.2 and 25.6 μN. The phase shift, due to the interaction of the CoCr coated silicon probe

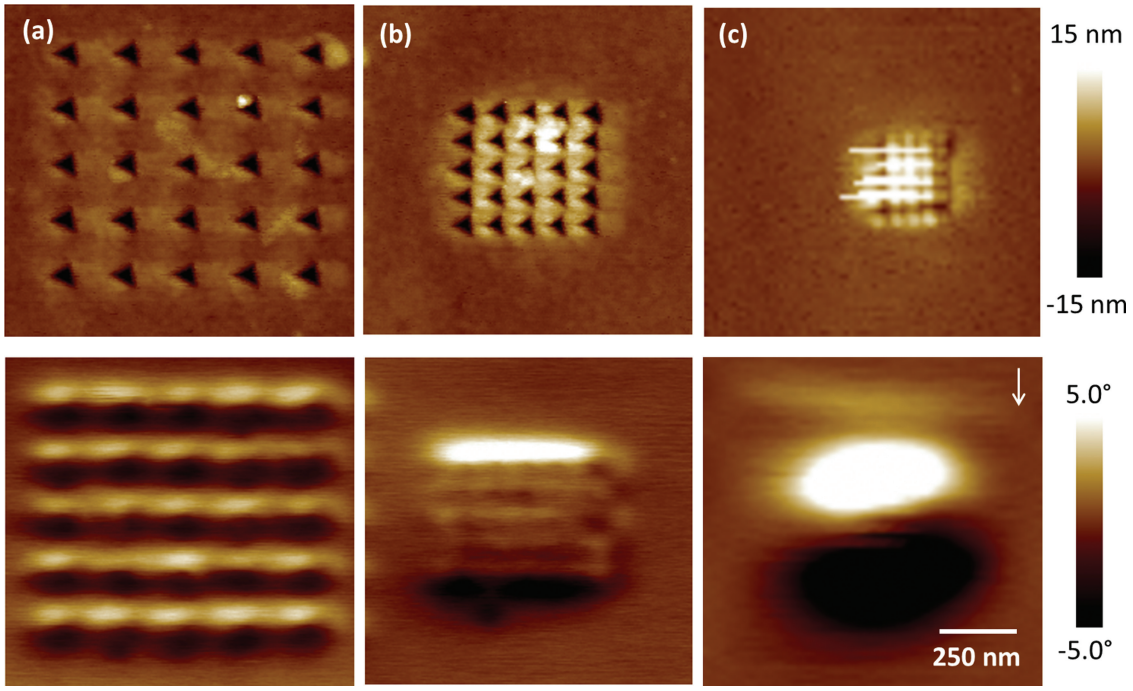


**Figure 4.** Topographical and MFM phase image of a a) 26 μN/200 nm array. where individual indentations begin to couple with the stray field of neighboring indentations; b) 26 μN/100 nm array with an enhanced bright/dark contrast at the top and bottom of the indentation array; and of a c) 26 μN/50 nm array. The magnetostatic coupling, represented by an enhanced magnetic stray field in (b) and (c), becomes more pronounced as the indentation spacing is decreased. For the 50 nm spacing, the plastically deformed regions of each indentation overlap with neighboring indentations. The streaks in the topography image (c) may be the result of the enhanced stray field interacting with the probe during imaging. The scale bar in (c) applies to all images in this figure.

with the magnetic stray field emanating from the indentations, decreased with decreasing load, from a full range of 10.5 to 7.8 to 4.0°, respectively. Figure 3e shows the relationship between the applied load and the magnetic contrast for the arrays in Figure 3c. To first order, the higher the indentation load, the more surface area is deformed, thus a greater amount of magnetic poles form, which results in a higher magnetic contrast. There is a balance between the magnitude of the applied load to obtain an appropriate contrast and the spacing to minimize magnetostatic coupling, which can be tuned to provide the information density needed for data storage applications.

Unlike the information storage capacity of isolated ferromagnetic single domain islands, which provide binary memory capacity due to magnetic anisotropy induced by arrays or by shape anisotropy, Ni-Mn-Ga exhibits high magnetocrystalline anisotropy enabling four magnetic memory states per cell (i.e., indentation). Magnetic information, by way of the magnetic poles stored about the locally deformed region, aligns to the magnetic moment. The strong magnetocrystalline anisotropy aligns the magnetic moment, and therefore the magnetic poles and magnetic stray field, parallel to the crystallographic *c* direction. The crystallographic *c* direction can be switched to one of two orthogonal axes *x* and *y* (**Figure 5**) through twin boundary motion facilitated by an appropriate applied magnetic field or mechanical stress orthogonal to the directionality of the dark/bright contrast. For each crystallographic state controlled by twin boundary motion, the magnetization vector can be magnetically switched 180° (Figure 5). Thus, by changing the magnetization direction through twin boundary motion, either with an applied magnetic field or stress-induced twin rearrangement, it is possible to formulate a four-state magnetic memory system. Supporting Information Figures S1-S3 not only demonstrate this phenomena, but also provide the framework to control the orientation of each individual cell. In particular, Figures S1a and S3 show twins intersecting indentations resulting in a 90° switch in the dark/bright contrast. The twin bands are relatively large and change the orientation of the magnetic stray field emanating from the intersected indentations. Thus, methods to control twinning and magnetization at the nanoscale are requisite to control the orientation of each individual cell independently of neighboring cells.

A critical component for data storage is data transfer rates. In 2003, working with less pure material with higher twinning stress than available today, Marioni et al. demonstrated a switching frequency of 2 kHz on a $5 \times 5 \times 8.95$ mm sample.[35] The switching frequency was limited by inertia, which implies an inverse cube dependence with linear size providing switching frequencies of $10^{15}$ Hz. Size effects of plastic deformation[36] are likely to limit the actuation frequency. A recent dynamical study on macroscopic samples revealed twin boundary velocities of ≈1 m/s for type II twins, which translates, on the nanometer length scale, to switching frequencies on the order of 1 GHz.[37] The practical limits for switching frequencies are yet to be determined.

For this work, a schema is established for the patterning of magnetic information on Ni-Mn-Ga with four stable, distinct

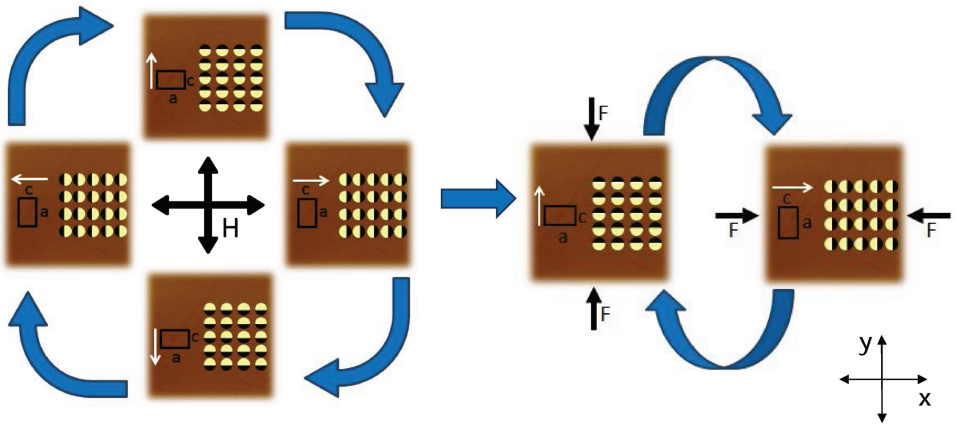


**Figure 5.** Schematic illustrating the four magnetic memory states. The orientation of the magnetic stray field, i.e., the dark/bright contrast sensed with MFM, can be globally controlled by applying a magnetic field or mechanical stress. Twin boundary motion switches the local magnetic stray field 90° through an applied magnetic field (outer cycle). A 180° switch of the magnetic stray field can be obtained by reversal of the magnetic field (inner intersection). A mechanical stress can also be applied, which results in the crystallographic *c* direction aligning parallel, but can be mutually opposite, to the direction of the applied force.

yet magnetically equivalent configurations. Ultimately, to achieve a 4 Tb/in$^2$ areal density in Ni-Mn-Ga, which is based on an 18 nm pitch, the magnetic stray field from an indentation must be resolved and distinguishable from a neighboring indentation. Recent developments with MFM probe spatial resolution, where sub-10 nm resolution has been demonstrated,[38,39] coupled with optimization of indenter tip geometry and indentation load could facilitate multi-Tb/in$^2$ storage capacity. Further, based on the mechanism to modify and control the orientation of the magnetic stray field, other surface modification techniques, for instance, focused ion beam, may be employed to exploit the formation of four magnetic states for high areal density storage applications.

## 3. Conclusions

In summary, i) the formation of nanoscale topological features through indentation-based techniques change the local magnetic contrast in Ni-Mn-Ga as demonstrated using AFM/MFM, ii) controlled, localized changes in magnetic stray field can be designed with indentation loads and spacing, iii) four magnetic-based memory states are defined due to magnetic field or stress-induced twin rearrangement along two crystal orientations, each with two possible magnetic orientations, iv) a schema is established for the patterning of magnetic information on Ni-Mn-Ga with four stable, distinct yet magnetically equivalent configurations and v) potentially, the four magnetic states and the controllable switching of those states, as reported here, could be used in quaternary non-volatile memory, as well as in Boolean operations. Such operations could lead to nanoscale information processing via magnetomechanical circuitry.

## 4. Experimental Section

Indentation, AFM and MFM experiments were performed on a parallelepiped Ni-Mn-Ga single crystal (AdaptaMat Ltd.) with 10 M martensite structure and martensite transformation temperatures above room temperature. The faces of the single crystal were parallel to the {100} planes. One face of the Ni-Mn-Ga single crystal was mechanically lapped with 1200 grit SiC paper and sequentially polished using 9, 3 and 1 μm diamond slurries and finished with a 0.3 μm alumina slurry. The single crystal was then electropolished for 15 s in 70 parts reagent alcohol and 30 parts nitric acid under a voltage of 2 VDC.

A scanning probe microscope (Dimension ICON and 3100, Nanoscope V Controller, Bruker Nano, Inc., Santa Barbara, CA) was used to perform nanoindentation and to measure topography and magnetic stray fields emanating from the surface. Indentations were made with a three-sided pyramidal diamond tip with a nominal radius of curvature of 40 nm (PDNISP, Bruker AFM Probes, Camarillo, CA). Topography and magnetic stray fields were imaged using CoCr coated silicon cantilevers (MESP, Bruker AFM Probes, Camarillo, CA). Prior to imaging, the CoCr probes were magnetized normal to the sample surface with the magnetization vector pointing toward the surface. AFM was performed using AC mode and MFM images were obtained using AC and constant height modes. Lift heights of 15–50 nm at scan rates of 0.5 to 1 Hz provided optimum resolution.

The indentation arrays were made using the diamond probe attached to a stainless steel cantilever. Indentation loads were based on the product of the spring constant and the deflection sensitivity of the stainless steel cantilever. The spring constant was provided by the probe manufacturer and the deflection sensitivity was measured on fused quartz. Indentation loads ranged from 5 to 128 μN with spacings from 25 to 750 nm. The indentation spacing was controlled using a X-Y closed-loop scanner.

A thermoelectric heating-cooling unit (Heater/Cooler System, Bruker Nano, Inc., Santa Barbara, CA) integrated with the AFM system was used to heat the Ni-Mn-Ga sample above the martensite phase transition temperature. To maximize thermal coupling to the thermoelectric stage, i) the sample was glued to a stainless steel puck using silver paint (Leitsilber 200, Ted Pella, Inc., Redding, CA) and ii) thermal paste was applied between the stainless steel puck and the thermoelectric stage. The sample was heated by ≈10 °C increments (with 5 min holds at each temperature) to 75 °C and held at temperature for 20 min to ensure complete transformation. The sample was then cooled to room temperature for additional imaging.

Indentation depths, before and after heating, were measured by taking cross-sections of each indentation. The same probe type, scan size, scan rate and pixel size were used to capture the images. A first order *x-y* plane fit was applied to the images. The recovery of the indentation

was measured as the difference between the maximum indentation depth before and after cooling over the maximum indentation depth before heating. The average recovery depth of 10 indentations with one standard deviation is given in the text.

## Supporting Information

Supporting Information is available from the Wiley Online Library or from the author.

## Acknowledgements

The authors thank Andrew Morrison for technical assistance. Financial support through the National Science Foundation under Grant No. CMMI-1068069 and DARPA Contract No. N66001-01-C-80345 is gratefully acknowledged.

Received: October 16, 2012
Revised: January 7, 2013
Published online: March 13, 2013

[1] P. Vettiger, G. Cross, M. Despont, U. Drechsler, U. Durig, B. Gotsmann, W. Haberle, M. A. Lantz, H. E. Rothuizen, R. Stutz, G. K. Binnig, *IEEE Trans. Nanotechnol.* **2002**, *1*, 39.
[2] C. H. Ahn, T. Tybell, L. Antognazza, K. Char, R. H. Hammond, M. R. Beasley, O. Fischer, J. M. Triscone, *Science* **1997**, *276*, 1100.
[3] S. Gidon, O. Lemonnier, B. Rolland, O. Bichet, C. Dressler, Y. Samson, *Appl. Phys. Lett.* **2004**, *85*, 6392.
[4] D. Wiesmann, C. Rawlings, R. Vecchione, F. Porro, B. Gotsmann, A. Knoll, D. Pires, U. Duerig, *Nano Lett.* **2009**, *9*, 3171.
[5] G. A. Shaw, J. S. Trethewey, A. D. Johnson, W. J. Drugan, W. C. Crone, *Adv. Mater.* **2005**, *17*, 1123.
[6] K. Ullakko, J. K. Huang, C. Kantner, R. C. Ohandley, V. V. Kokorin, *Appl. Phys. Lett.* **1996**, *69*, 1966.
[7] A. Sozinov, A. A. Likhachev, N. Lanska, K. Ullakko, *Appl. Phys. Lett.* **2002**, *80*, 1746.
[8] P. Müllner, V. A. Chernenko, G. Kostorz, *Scr. Mater.* **2003**, *49*, 129.
[9] L. Straka, N. Lanska, K. Ullakko, A. Sozinov, *Appl. Phys. Lett.* **2010**, *96*, 131903.
[10] L. Straka, O. Heczko, *Scr. Mater.* **2006**, *54*, 1549.
[11] L. Straka, A. Soroka, H. Seiner, H. Hanninen, A. Sozinov, *Scr. Mater.* **2012**, *67*, 25.
[12] J. M. Howe, R. C. Pond, J. P. Hirth, *Prog. Mater. Sci.* **2009**, *54*, 792.
[13] O. Heczko, *J. Magn. Magn. Mater.* **2005**, *290*, 787.
[14] G. Li, Y. Liu, B. K. A. Ngoi, *Scr. Mater.* **2005**, *53*, 829.
[15] L. Straka, O. Heczko, *J. Magn. Magn. Mater.* **2005**, *290*, 829.
[16] A. Pramanick, K. An, A. D. Stoica, X. L. Wang, *Scr. Mater.* **2011**, *65*, 540.
[17] I. Aaltio, X. W. Liu, M. Valden, K. Lahtonen, O. Söderberg, Y. Ge, S. P. Hannula, *J. Alloys Compd.* **2012**, In Press.
[18] Y. Ganor, D. Shilo, *Appl. Phys. Lett.* **2008**, *93*, 031905.
[19] C. Liu, Z. Y. Gao, X. An, H. B. Wang, L. X. Gao, W. Cai, *Appl. Surf. Sci.* **2008**, *254*, 2861.
[20] P. Müllner, Z. Clark, L. Kenoyer, W. B. Knowlton, G. Kostorz, *Mater. Sci. Eng. A* **2008**, *481*, 66.
[21] A. M. Jakob, M. Müller, B. Rauschenbach, S. G. Mayr, *New J. Phys.* **2012**, *14*, 033029.
[22] C. E. Betz, *Principles of Magnetic Particle Testing*, Magnaflux Corp., Chicago, IL **1967**.
[23] F. Bitter, *Phys. Rev.* **1931**, *38*, 1903.
[24] H. J. Williams, R. M. Bozorth, W. Shockley, *Phys. Rev.* **1949**, *75*, 155.
[25] A. Wadas, H. J. Guntherodt, *J. Appl. Phys.* **1990**, *68*, 4767.
[26] M. Lohndorf, R. Wiesendanger, *Appl. Phys. A* **1995**, *61*, 93.
[27] N. Scheerbaum, Y. W. Lai, T. Leisegang, M. Thomas, J. Liu, K. Khlopkov, J. McCord, S. Fahler, R. Trager, D. C. Meyer, L. Schultz, O. Gutfleisch, *Acta Mater.* **2010**, *58*, 4629.
[28] R. S. Tebble, *Magnetic Domains*, Methuen, London **1969**.
[29] A. Hubert, R. Schäfer, *Magnetic Domains: The Analysis of Magnetic Microstructures*, Springer, Berlin, New York **1998**.
[30] R. P. Cowburn, M. E. Welland, *Science* **2000**, *287*, 1466.
[31] J. I. Martin, J. Nogues, K. Liu, J. L. Vicent, I. K. Schuller, *J. Magn. Magn. Mater.* **2003**, *256*, 449.
[32] R. F. Wang, C. Nisoli, R. S. Freitas, J. Li, W. McConville, B. J. Cooley, M. S. Lund, N. Samarth, C. Leighton, V. H. Crespi, P. Schiffer, *Nature* **2006**, *439*, 303.
[33] J. W. Lau, J. M. Shaw, *J. Phys. D-Appl. Phys.* **2011**, *44*, 303001.
[34] A. Imre, G. Csaba, L. Ji, A. Orlov, G. H. Bernstein, W. Porod, *Science* **2006**, *311*, 205.
[35] M. A. Marioni, R. C. O'Handley, S. M. Allen, *Appl. Phys. Lett.* **2003**, *83*, 3966.
[36] M. D. Uchic, D. M. Dimiduk, J. N. Florando, W. D. Nix, *Science* **2004**, *305*, 986.
[37] E. Faran, D. Shilo, *Appl. Phys. Lett.* **2012**, *100*, 151901.
[38] L. M. Belova, O. Hellwig, E. Dobisz, E. D. Dahlberg, *Rev. Sci. Instrum.* **2012**, *83*, 093711.
[39] M. Ohtake, K. Soneta, M. Futamoto, *J. Appl. Phys.* **2012**, *111*, 07e339.